Phospho-regulated tuning of viscoelastic properties balances centrosome growth and strength

Matthew Amato[1], June Ho Hwang[2], Manolo U. Rios[1], Nicole E. Familiari[1], Michael K. Rosen[2], Jeffrey B. Woodruff[1,3]

1. Dept. of Cell Biology, UT Southwestern Medical Center, Dallas, TX 75390, USA
2. Dept. of Biophysics, Howard Hughes Medical Institute, UT Southwestern Medical Center, Dallas, TX 75390, USA
3. For correspondence: jeffrey.woodruff@utsouthwestern.edu

SIGNIFICANCE STATEMENT

To build and position the mitotic spindle, centrosomes must grow large enough to nucleate many hundreds of microtubules and resist their pulling forces. How centrosomes simultaneously achieve dynamic growth and tensile strength is unknown. Here, we show that centrosomes behave as phosphorylation-tunable hydrogels with both liquid-like and solid-like properties, which contribute to dynamics and material strength, respectively. Phospho-null or phospho-mimicking mutations in the scaffold protein SPD-5 dysregulate the balance of liquid- and sold-like behaviors within the centrosome, impairing function and embryo viability in both cases. Our results showcase how meso-scale material properties contribute to the function of a membrane-less organelle and how they are finely tuned by chemical modifications.

ABSTRACT

Centrosomes nucleate microtubule asters and comprise centrioles surrounded by pericentriolar material (PCM). In preparation for mitosis, the PCM scaffold grows dramatically while resisting microtubule pulling forces. How PCM achieves dynamic growth while maintaining mechanical strength is unclear. Here we probed the dynamic and material properties of the *C. elegans* PCM scaffold. Single-embryo extrusion experiments revealed that the protein SPD-5 forms distinct but co-existing dynamic and stable scaffolds within PCM. The stable scaffold grew in preparation for mitosis, then

disappeared at anaphase onset. SPD-5 mutants that lacked PLK-1 phosphorylation at four key sites (4A) could not build the stable scaffold, whereas phospho-mimetic SPD-5(4E) could. Expression of SPD-5(4A) impaired PCM assembly, but this phenotype was partially rescued by eliminating microtubule pulling forces, indicating material weakness. SPD-5(4A) expression also resulted in chromosome segregation defects, revealing the importance of PCM strength for development. Unexpectedly, expression of SPD-5(4E) prevented full-scale PCM growth and caused embryonic lethality. *In vitro*, PLK-1-induced phosphorylation increased the viscoelastic moduli of minimal SPD-5 scaffolds, which increased their solidity. This caused faster initial growth that then plateaued, in effect setting an upper limit to SPD-5 scaffold size. Thus, PCM scaffold assembly and strength are optimized through phospho-regulated equilibrium of dynamic and stable scaffold components. Our results further reveal kinase-driven kinetic arrest as a potential mechanism of centrosome size scaling.

INTRODUCTION

The centrosome is a membrane-less organelle composed of centrioles that organize a micron-scale mass of protein called pericentriolar material (PCM). Upon entry into mitosis, PCM rapidly expands by accumulating scaffold proteins that then recruit client proteins (e.g., gamma-tubulin) needed for microtubule aster formation (Gomes Pereira et al., 2021). The scaffold proteins have been unambiguously identified in nematodes (SPD-5) and insects (Cnn) and contain numerous coiled-coil domains interspersed with disordered linkers (Hamill et al., 2002; Megraw et al., 1999). Polo-Like Kinase phosphorylation potentiates centrosome maturation by promoting the self-association of these scaffold proteins (Conduit et al., 2014; Rios et al., 2024; Woodruff et al., 2015). Proper microtubule organization at the centrosome is important for the formation of the mitotic spindle, which segregates mitotic chromosomes during cell division. Centrosomes also nucleate astral microtubules that connect to cortically anchored motors, which generate force to position the mitotic spindle (Laan et al., 2012; Pecreaux et al., 2006). How PCM achieves mechanical strength to resist these forces while simultaneously incorporating new scaffolding material remains unclear.

While key molecular interactions driving PCM scaffold assembly have been identified (Feng et al., 2017; Nakajo et al., 2022; Rios et al., 2024; Wang et al., 2010), a quantitative assessment of PCM material properties is currently lacking. This has led to uncertainties and contradictory conclusions concerning the physical nature of PCM. On the one hand, some studies suggest that PCM is a solid-like material. For example, electron microscopy of isolated centrosomes from the Atlantic surf clam and cryo-electron tomography of native centrosomes in *C. elegans* embryos revealed that a lattice-like network undergirds PCM (Schnackenberg et al., 1998; Tollervey et al., 2024). Fluorescence recovery after photobleaching (FRAP) experiments indicated little turnover within the mature PCM scaffold in *D. melanogaster* and *C. elegans* embryos (Conduit et al., 2014; Laos et al., 2015). Taken together, these observations demonstrate that the PCM contains a static structure, supporting the notion that PCM scaffold is a lattice-like matrix. On the other hand, evidence for a dynamic PCM scaffold exists, albeit circumstantially. Laos et al. (2015), reported a minor mobile fractionafter photobleaching of GFP-labeled SPD-5 in *C. elegans* embryos (~10% recovery after 65 s). However, in this experiment it is difficult to distinguish the effects of incorporating new material (i.e., growth) from material exchange or rearrangement. Biochemical reconstitution revealed that SPD-5 forms micron-scale spherical condensates in the presence of a molecular crowding agent (Woodruff et al., 2017). This study proposed that the SPD-5 scaffold is initially liquid-like and then rapidly ages into a non-dynamic state. It is not known to what extent this minimal system faithfully recapitulates native PCM properties. Finally, optical nano-rheology showed that PCM can flow under shear stress, but only during its disassembly phase or when PLK-1 is inhibited (Mittasch et al., 2020). It is unclear if a dynamic scaffolding component contributes to PCM assembly in unperturbed cells. Thus, it is important to clarify 1) the extent to which PCM contains static and dynamic scaffolding, 2) how these scaffolds contribute to mesoscale properties like viscosity, elasticity, and strength, and 3) how these features are regulated and contribute to cell viability.

Here we used cell-based and *ex vivo* biophysical assays, biochemical reconstitution, and microrheology to characterize the material states of *C. elegans* PCM and how they are regulated by PLK-1 phosphorylation. We show that SPD-5 can transition between dynamically and stably associated states based on its phosphorylation

status. The stable scaffold contributes to PCM strength, while the dynamic scaffold contributes to PCM growth and achieving a spherical morphology.

RESULTS

The *C. elegans* PCM scaffold is a composite of distinct but coexisting static and dynamic components

Analysis of PCM dynamics during its growth phase is difficult to interpret due to strong contributions from newly incorporated material from the cytoplasm. We thus used controlled extrusion to assess PCM scaffold properties while avoiding the confounding effects of growth. By coating *C. elegans* embryos with calcofluor white, a fluorescent dye that binds chitin and absorbs blue light, we could use a short, focused pulse of 405 nm laser light to create precise punctures. Application of light pressure forces the PCM (labeled with GFP::SPD-5) out of the embryo into a dilute, controlled medium (Figure 1A). When extruded into low salt buffer (25 mM HEPES, 0 KCl), PCM remained mostly intact for >1 hr (Figure 1B). Thus, the PCM scaffold is intrinsically stable and does not require cytoplasmic factors for its maintenance in low salt conditions.

We hypothesized that if the PCM scaffold is a solid, stable matrix, it should be relatively insensitive to dilution into a near-physiological salt buffer (25 mM HEPES, 150 mM KCl). However, if the PCM scaffold is a dynamic, liquid-like phase, it should rapidly dissolve after dilution in the same buffer. Use of extrusion allowed distinction of solid-like and liquid-like phases of P granules, indicating its applicability (Putnam et al., 2019). Extrusion into physiological salt buffer caused dissipation of GFP::SPD-5 signal, both in area and mean intensity. In extruded interphase and metaphase cells, GFP signal rapidly declined initially and then plateaued. In extruded anaphase cells, GFP signal monotonically decreased until PCM was completely dissolved (Figure 1C-E). Thus, PCM in the dilute solution is unstable due to a dynamic fraction of SPD-5 that departs. We term this fraction the “dynamic component”. The remaining salt-insensitive fraction of GFP::SPD-5 seen in interphase and metaphase cells was stable for 1 hr. We term this population of SPD-5 the “stable component”. The stable component was smallest in interphase, larger in metaphase, and non-existent in anaphase. (Figure 1D). These

121 results reveal that dynamic and stable pools of SPD-5 co-exist within PCM. The dynamic
122 component is present throughout the cell cycle, whereas the stable component grows in
123 preparation for mitosis, then disappears after anaphase entry. The co-existence of these
124 dynamically different scaffold populations might explain the discrepancies in the literature
125 about the material nature of PCM (see discussion).

126 **Phosphorylation of SPD-5 regulates the equilibrium of the dynamic and static PCM**
127 **scaffold components**

128 Our results indicate that the relative fractions of static and dynamic PCM scaffold
129 components differ during the cell cycle, suggesting regulation (Fig 1B, C). We
130 hypothesized that PLK-1 phosphorylation of SPD-5 could determine its dynamic
131 properties. We thus generated embryos that express GFP-tagged transgenes of *spd-5*
132 from an ectopic locus in the genome (Woodruff et al., 2015). These transgenes were re-
133 encoded to be RNAi-resistant, thus allowing us to study their effects after depletion of
134 endogenous *spd-5*. We mutated four residues known to be phosphorylated by PLK-1
135 (S530, S627, S653, S658) to alanine (4A; phospho-null) or glutamic acid (4E; phospho-
136 mimetic) (Figure 2A). We analyzed one-cell embryos in metaphase, as these have the
137 largest PCM that contains both the stable and dynamic SPD-5 components. Mitotic PCM
138 built from these SPD-5 variants showed different sensitivities to dilution when extruded:
139 compared to wild-type SPD-5, GFP::SPD-5(4E) showed an increased persistence at the
140 centrosome, whereas GFP::SPD-5(4A) rapidly dispersed (Figure 2B). These results
141 suggest that phosphorylated SPD-5 produces the stable component, while
142 unphosphorylated SPD-5 produces the dynamic component.

143 We then assayed how the phosphorylation state of SPD-5 affects PCM scaffold
144 dynamics in intact embryos by performing partial FRAP. We selected embryos at nuclear
145 envelope breakdown (NEBD), when the PCM is large enough to perform partial FRAP
146 and there is enough time to take measurements before natural PCM disassembly occurs
147 in anaphase (>150 s). GFP::SPD-5(WT) showed almost no detectable recovery over 100
148 s, as expected for this timescale (Laos et al., 2015). GFP::SPD-5(4E) signal also did not
149 recover, whereas GFP::SPD-5(4A) signal did (Figure 2C). Thus, SPD-5(4A) is dynamic
150 and exchanges between the PCM and surroundings, consistent with our extrusion

experiments. The inability of FRAP to resolve differences between SPD-5(WT) and SPD-5(4E) indicates that extrusion is a more sensitive assay of dynamics, likely because it operates on longer time scales (20-40 min). We conclude that phosphorylation of SPD-5 decreases its dynamics within PCM and promotes the formation of the stable PCM component.

PLK-1 phosphorylation changes the dynamics of reconstituted PCM scaffolds

We next tested if PLK-1 phosphorylation is sufficient to modify the dynamic properties of the SPD-5 scaffold. We reconstituted minimal SPD-5 scaffolds and investigated their material properties in the presence and absence of PLK-1 phosphorylation. Previous reconstitution of spherical SPD-5 condensates required the use of the crowding agent PEG, which severely dampened regulation by PLK-1 (Woodruff et al., 2017). To circumvent these complications, we discovered conditions that permit SPD-5 condensation without using a macromolecular crowding agent. We found that SPD-5 in combination with its client protein TPXL-1 will condense into micron-scale droplets at low salt concentrations (75 mM KCl; Figure 3A, S1A,B). We then incubated SPD-5/TPXL-1 condensates with constitutively-active (CA) or kinase dead (KD) PLK-1 in the presence of 0.4 mM ATP for 30 minutes. After incubation with PLK-1(KD), condensates remained dynamic and could fuse (Figure 3B). FRAP revealed recovery of both the SPD-5::RFP and TPXL-1::GFP signal (Figure 3C; S1C). On the other hand, condensates incubated with PLK-1(CA) did not dynamically rearrange nor could they fuse (Figure 3B); instead, these condensates formed chains reminiscent of colloidal gels. Under these conditions, SPD-5::RFP signal did not recover after photobleaching, while TPXL-1::GFP signal recovered fully (Figure 3C). These results suggest that phosphorylation-driven reduction of condensate dynamics is due to the stabilization of SPD-5. Unphosphorylated condensates lost considerable mass upon 4.3X dilution into extrusion buffer (150mM KCl, 25mM Hepes pH 7.4), whereas phosphorylated condensates maintained their mass (Figure 3D). These data indicate that PLK-1 phosphorylation directly decreases the dynamics and increases the stability of the SPD-5 scaffold. These results are consistent with our *in vivo* FRAP and extrusion analyses, highlighting the physiological relevance of our simplified reconstitution system.

182

183 **Phosphorylation increases the viscoelasticity of reconstituted PCM scaffolds**

184 To quantify how phosphorylation changes the material properties of reconstituted
185 PCM, we performed video particle tracking micro-rheology (VPT) of 100 nm fluorescent
186 beads embedded in SPD-5/TPXL-1 condensates incubated with PLK-1(CA) or PLK-
187 1(KD) (Figure 4A). To minimize effects from confinement, only beads located in the
188 condensate center were analyzed (see methods). Phosphorylation reduced the mean
189 squared displacement (MSD) of beads inside the condensates (n>17,000 trajectories;
190 Figure 4B). Using the Generalized Stokes-Einstein Relation, we expressed MSD in terms
191 of the viscoelastic modulus, which consists of viscous (G”) and elastic (G’) moduli as
192 functions of frequency (ω) (Figure 4C). Phosphorylation shifted the crossover point
193 between G’ and G’’ upward, indicating a transition to higher viscoelasticity (Figure 4C),
194 and to the left, indicating emergence of elastic (solid-like) behavior at lower frequencies.
195 Next, we derived viscosity (η) as a function of frequency using the relation η=G”/ω.
196 Phosphorylation increased the condensate viscosity at all frequencies (Figure 4D). The
197 estimated zero-shear viscosity (resting viscosity) of the condensates differed nearly 10-
198 fold: 31.8 Pa*s in the presence of PLK-1(CA) vs. 3.8 Pa*s in the presence of PLK-1(KD).

199 The response of a viscoelastic material is dominated by elastic contributions on
200 short time scales and viscous contributions on longer time scales. Relaxation time
201 characterizes the timescale when a material transitions from elastic to viscous behavior
202 under applied stress, and it is defined as the inverse of the frequency at the G’-G”
203 crossover point. Longer relaxation times are associated with more elastic, solid-like states.
204 Phosphorylation increased the relaxation time of SPD-5/TPXL-1 condensates (4.6 s (CA)
205 vs.1.03 s (KD))(Figure 4E). Our micro-rheology data, combined with FRAP and fusion
206 assays, indicate that PLK-1 phosphorylation directly increases the viscoelasticity of the
207 PCM scaffold and makes its behavior more solid-like.

208

209 **<u>Hypo-phosphorylation of SPD-5 impairs PCM strength and the fidelity of</u>**
210 **<u>chromosome segregation</u>**

211 Our data so far indicate that phosphorylation tunes the material properties of the
212 PCM scaffold. We next investigated how dysregulation of SPD-5 phosphorylation impacts

213 PCM function in living embryos. Expression of GFP::SPD-5(4A) in the absence of
214 endogenous WT SPD-5 impaired PCM assembly, as expected (Woodruff et al., 2015).
215 Based on our *in vitro* data and prior work (Lucas and Raff, 2007; Rios et al., 2024), we
216 hypothesized that this assembly defect could be a material phenotype, such that PCM
217 can assemble but is too weak to resist microtubule-dependent pulling forces. In *spd-5(4A)*
218 interphase embryos, depolymerizing microtubules with 40 μM nocodazole increased
219 PCM scaffold mass 2.7-fold ($p<0.005$)(Figure 5A). PCM mass in control embryos was not
220 significantly affected by nocodazole (1.2-fold change; $p = 0.24$). Since microtubule-
221 dependent pulling forces stretch PCM, nocodazole treatment reduced PCM area in *spd-*
222 *5(WT)* embryos. Conversely, nocodazole addition increased PCM area in *spd-5(4A)*
223 embryos, likely due to increased accumulation of SPD-5(4A) in the absence of forces
224 (Figure 5A). Thus, hypo-phosphorylated SPD-5 can build PCM, but it is weak and
225 dissembled by pulling forces. Since SPD-5(4A) only forms the dynamic scaffold, this
226 result suggests that the stable scaffold is essential for PCM strength.
227 Expression of SPD-5(4A), but not SPD-5(WT), caused embryo lethality and
228 chromosome segregation defects in all embryos imaged (n=16). Phenotypes included
229 lagging chromosomes, micronuclei multiple nuclei, chromosome separation failure during
230 metaphase, and multipolar spindles (Figure 5B, C). Previous work demonstrated that
231 achieving full-sized PCM is not essential for accurate chromosome segregation (Ohta et
232 al., 2021). Thus, we speculate that these phenotypes in *spd-5(4A)* embryos are likely not
233 due to defects in PCM size, but rather to defects in PCM strength.
234
235 **Hyper-phosphorylation of SPD-5 limits PCM scaffold growth**
236 Several studies have shown that PLK-1 potentiates assembly of the PCM (Conduit
237 et al., 2014; Decker et al., 2011; Haren et al., 2009; Lee and Rhee, 2011; Woodruff et al.,
238 2015). A key prediction is that PCM assembly should scale with the degree of
239 phosphorylation. To the contrary, we observed that PCM built with SPD-5(4E) was
240 smaller than the controls (Figure 6A,B). We often observed small foci of GFP::SPD-5(4E)
241 separate from the main PCM body in embryos depleted of endogenous SPD-5 (Figure
242 6B); these foci could represent ectopically nucleated complexes, as seen with phospho-
243 mimetic Cnn mutants in *D. melanogaster* (Conduit et al., 2014). Even including these

244 ectopic foci, the overall mass of detected PCM was still smaller in 4E vs. WT embryos
245 (Figure 6B). This difference in size remained even after treatment with nocodazole,
246 demonstrating that hyperphosphorylation limits PCM growth in a force-independent
247 manner (Figure 6C). SPD-5(4E) levels were slightly higher than SPD-5(WT) (Figure S2A);
248 thus, differences in PCM size were not due to decreased transgene expression.
249 Furthermore, centrosome size is known to be affected by cell cycle length in flies (Wong
250 et al., 2024); however, we did not observe significant changes in cell cycle length between
251 embryos solely expressing GFP::SPD-5(WT) and GFP::SPD-5(4E) (+RNAi conditions;
252 Figure S2B).

253 Expression of GFP::SPD-5(4E) caused smaller, irregularly shaped centrosomes
254 but did not result in chromosome segregation defects during early embryogenesis (Figure
255 6D). 34% embryos expressing GFP::SPD-5(4E) did not hatch, indicating that SPD-5
256 hyper-phosphorylation interferes with late embryonic development (Figure 6E). We
257 conclude that hyper-phosphorylation of SPD-5 promotes its initial self-assembly but
258 hinders PCM growth, ultimately leading to pathologically stable PCM and failed embryonic
259 development.

260 We next tested if hyperphosphorylation is sufficient to limit PCM scaffold growth.
261 We observed a biphasic behavior in our *in vitro* condensate assembly assay: at early time
262 points, phosphorylation promoted SPD-5 condensate assembly; later, phosphorylation
263 inhibited condensate growth (Figure 6F). Our results support a model where PLK-1
264 activity promotes the initial assembly of SPD-5 but, if unchecked, leads to premature
265 termination of assembly.

266

267 **Discussion**

268 In preparation for mitotic spindle assembly, the protein-rich PCM must perform two
269 seemingly contradictory behaviors: it must be stable enough to resist microtubule-
270 dependent forces and dynamic enough to grow. Our results suggest that these behaviors
271 are enabled due to the tunable viscoelastic nature of the PCM scaffold. The main scaffold
272 protein in *C. elegans*, SPD-5, is likely under-phosphorylated when it first incorporates into
273 PCM. In this state, SPD-5 is dynamic and can rearrange and depart, creating a viscous,
274 liquid-like scaffold that favors isotropic growth and the spherical morphology characteristic

275 of PCM (Laos et al., 2015). Active PLK-1 concentrated within PCM phosphorylates SPD-
276 5, causing a transition to an elastic, solid-like network that confers strength. The two SPD-
277 5 scaffold components co-exist *in vivo*, presumably due to the competition between
278 phosphorylation by PLK-1 and de-phosphorylation by PP2A, a PCM-resident
279 phosphatase (Enos et al., 2018; Magescas et al., 2019). Dysregulation of this competition
280 is pathological: under-phosphorylation creates PCM that is too dynamic and weak,
281 leading to premature PCM disassembly and chromosome segregation errors, while over-
282 phosphorylation creates PCM that is too stable and irregular in size and shape (Figure 7).
283 How might phosphorylation regulate the material properties and size of the SPD-
284 5 scaffold? Our previous work revealed that SPD-5 forms supramolecular assemblies
285 through multivalent coiled-coil interactions (Rios et al., 2024). Phosphorylation blocks
286 auto-inhibitory interactions, opening up SPD-5 so that coiled-coil domains can interact in
287 trans, which would promote scaffold growth. Our in vitro rheology revealed that
288 phosphorylation directly increased the viscoelasticity of SPD-5 scaffolds, making them
289 more solid-like. In vivo, expression of SPD-5(4A) led to weaker PCM (Figure 5). These
290 results suggest that PCM strength is derived from PLK-1-induced solidification of the
291 SPD-5 scaffold.
292 As it is well established that PLK-1 phosphorylation is essential for mitotic PCM
293 assembly (Conduit et al., 2014; Decker et al., 2011; Haren et al., 2009; Lee and Rhee,
294 2011; Woodruff et al., 2015), it was surprising that hyper-phosphorylation of SPD-5 led to
295 PCM that was smaller than normal (Figure 6A-E). *In vitro*, PLK-1 phosphorylation initially
296 promoted SPD-5 assembly, as expected, but then arrested growth, in effect capping SPD-
297 5 size at a set limit (Figure 6F). How could PLK-1 phosphorylation of SPD-5 both promote
298 and limit its assembly? One hypothesis is that phosphorylation of SPD-5 creates inter-
299 molecular interactions that are too strong and are unable to release and bind new
300 molecules. Eventually, all possible interaction motifs would be occupied, thus preventing
301 the addition of new molecules and capping growth. Simulations of ideal multivalent
302 polymers demonstrated that this mechanism, termed “valency exhaustion”, is sufficient to
303 cause kinetic arrest and stop condensate growth (Ranganathan and Shakhnovich, 2020).
304 Alternatively, it is possible that hyper-phosphorylation promotes excessive nucleation of
305 small, ectopic SPD-5 scaffolds that are too solidified to fuse together; these nuclei could

306 soak up the available pool of bulk SPD-5, thus stalling growth of the main PCM body. We
307 could detect some ectopic SPD-5(4E) scaffolds; however, even after including them in
308 our calculations, PCM mass was still smaller in embryos expressing SPD-5(4E) vs. SPD-
309 5(WT)(Figure 6B). Still, we cannot exclude the possibility of many smaller ectopic
310 complexes that cannot be detected by light microscopy. Regardless of the exact
311 molecular basis of this phenomenon, we propose that phosphorylation-induced kinetic
312 arrest strengthens PCM and sets its upper size limit. Future work will assess how tuning
313 of scaffold dynamics and material properties contribute to developmental size scaling of
314 PCM (Decker et al., 2011) and other membrane-less organelles.

315 Our work indicates that PCM is organized as a solid phase intercalated by a liquid-
316 like phase of proteins. This model is consistent with the observations that *C. elegans* PCM
317 is spherical and grows isotopically (Laos et al., 2015), which is expected for a viscous
318 liquid, but also contains an underlying fibrous meshwork (Tollervey et al., 2024), which
319 would be expected for an elastic solid. These features are reminiscent of polymer-based
320 hydrogels (Sun et al., 2013). Recently, it was shown that PCM in *D. melanogaster*
321 embryos is also a composite of a stable scaffold composed of Cnn co-existing with a
322 dynamic phase of TACC protein, both of which can assemble independently of the other
323 (Wong and Raff 2024). The Cnn scaffold seems to be important for mechanical strength
324 (Lucas and Raff, 2007), while the TACC scaffold is required to recruit specific clients
325 (Wong and Raff 2024). While the identities of the PCM scaffolding components differ
326 between species, it is possible that the overall material design—a viscoelastic hydrogel—
327 may be conserved.

328 More broadly, our work demonstrates how tuning material properties is required
329 for proper biological function of a membrane-less organelle. Liquidity allows isotopic
330 incorporation and rearrangement of new scaffolding material, which are important for
331 PCM to reach its full size and microtubule-nucleating capacity. Solidification of the PCM
332 scaffold creates strength so that it can maintain integrity under microtubule-mediated
333 pulling forces that position the spindle and move mitotic chromosomes. Based on studies
334 of polyampholyte hydrogels (Sun et al., 2013), the combination of strongly- and weakly-
335 associated scaffold molecules is ideal for creating a material that is both tough and
336 resistant to repeating pulling forces (i.e., fatigue). Weak interactions allow for minor

rearrangements that dissipate energy over time and self-heal, while the strong interactions maintain the overall form of the structure (Sun et al., 2013). This finding contrasts with most studies on condensates and other supramolecular assemblies, such as FUS droplets, TDP-43 aggregates, and amyloids, which propose that solidification is pathological (Alberti and Hyman, 2021). Thus, our study joins a growing body of work revealing that solidification can be physiological when condensates are required to resist mechanical stresses (Mittasch et al., 2020) or shut down biochemistry (Boke et al., 2016; Bose et al., 2022).

ACKNOWLEDGEMENTS

We thank Jessica Feldman for advice on performing embryo laser extrusion, Jordan Raff for advice on *in vivo* experiments, and Anthony Hyman for antibodies.

DATA AVAILABILITY

Further requests and information for resources and reagents should be directed to and will be fulfilled by the Lead Contact, Jeffrey Woodruff (Jeffrey.woodruff@utsouthwestern.edu).

COMPETING INTERESTS

The authors declare no competing interests.

FUNDING

J.B.W. is supported by an R35 grant from the National Institute of General Medical Sciences (1R35GM142522) and the Endowed Scholars program at UT Southwestern. M.A. was supported by a National Research Service Award T32 (GM131963).

AUTHOR CONTRIBUTIONS

M. Amato performed all experiments and analyzed data. J.H. Hwang performed VPT analysis. M.U. Rios developed and optimized the embryo extrusion assay and performed and analyzed extrusion experiments. N.E. Familiari made baculoviruses and expressed

364 proteins. J.B. Woodruff made transgenic *C. elegans* strains. M. Amato and J.B. Woodruff
365 wrote the manuscript. J.B. Woodruff supervised the project.

366 MATERIALS AND METHODS

367 Experimental model and subject details

368 For the expression of recombinant proteins (listed in Table S1), we used SF9-ESF *S.*
369 *frugiperda* insect cells grown at 27°C in ESF 921 Insect Cell Culture Medium (Expression
370 Systems) supplemented with Fetal Bovine Serum (2% final concentration). *C. elegans*
371 worm strains were grown on nematode growth media (NGM) plates at 23°C, following
372 standard protocols (www.wormbook.org). Worm strains used in this study are listed in
373 Table S2.

374 Generation of transgenic *C. elegans*

375 *C. elegans* worm strains used in this study were created with MosSCI (Frokjaer-Jensen
376 et al., 2008) and are based on constructs made previously (Woodruff et al., 2015).
377 GFP::SPD-5(4E) mutant was created by replacing a section of the wild-type sequence
378 with a mutated gene block. All plasmids were purified using a NucleoBond Xtra Midi Prep
379 Kit (Macherey Nagel), combined with co-injection plasmids, and injected into strain
380 EG6699 (tt5605, Chr II). After one week, worms were heat-shocked for 3 hr at 35°C to kill
381 worms maintaining extrachromosomal arrays. Moving worms without fluorescent co-
382 injection markers were selected as candidates. Sequencing was used to confirm
383 transgene integration.

384 Protein purification

385 All expression plasmids are listed in Table S1. SPD-5, TPXL-1 and PLK-1 constructs were
386 expressed and purified as previously described (Woodruff et al., 2017; Woodruff and
387 Hyman, 2015; Woodruff et al., 2015). Baculoviruses were generated using the FlexiBAC
388 system (Lemaitre et al., 2019) in SF9 cells. Protein was harvested 72 hr after infection
389 during the P3 production phase. Cells were collected, washed, and resuspended in
390 harvest buffer (25 mM HEPES, pH 7.4, 150 mM NaCl). All subsequent steps were

391 performed at 4°C. Cell pellets were resuspended in buffer A (25 mM HEPES, pH 7.4, 30
392 mM imidazole, 500 mM KCl, 0.5 mM DTT, 1% glycerol, 0.1% CHAPS) + protease
393 inhibitors and then lysed using a dounce homogenizer. Proteins were bound to Ni-NTA
394 (Qiagen), washed with 10 column volumes of buffer A, and eluted with 250 mM imidazole.
395 For SPD-5 proteins, Ni-NTA eluate was then bound to MBP-Trap beads (Chromotek) and
396 washed with 5 column volumes of buffer A and eluted with by adding PreScission
397 protease, incubating overnight and then passing over Ni-NTA to remove the Precission
398 protease. For TPXL-1 proteins, Ni-NTA eluate was equilibrated with binding buffer (25
399 mM HEPES, pH 7.4, 150 mM KCl) and then bound to SP Sepharose (GE Healthcare
400 catalog No: 10261262) and washed with 5 column volumes of binding buffer. TPXL-1 was
401 eluted using buffer A. For PLK-1 proteins, Ni-NTA eluate was concentrated with a 30 K
402 MWCO Amicon concentrator (Millipore), filtered, and then passed over a Superdex 75
403 increase size exclusion column (Cytiva). Purified proteins were then concentrated using
404 30 K MWCO Amicon concentrators (Millipore). All proteins were aliquoted in PCR tubes,
405 flash-frozen in liquid nitrogen, and stored at −80°C. Protein concentration was determined
406 by measuring absorbance at 280 nm using a NanoDrop ND-1000 spectrophotometer
407 (Thermo Fisher Scientific).

408 **RNAi treatment**

409 RNAi was done by feeding. The *spd-5* feeding clone targets a region that is reencoded in
410 our MosSCI transgenes (Woodruff et al., 2015). Bacteria were seeded onto nematode
411 growth media (NGM) supplemented with 1 mM isopropyl β-D-1-thiogalactopyranoside
412 (IPTG) and 100 µg/mL ampicillin. L4 hermaphrodites were grown on feeding plates at
413 23°C for 24-30 hr.

414 Target sequence for *spd-5(RNAi)*

415 5′-TGG AAT TGT CCG CTA CTG ATG CAA ACA ACA CAA CTG TCG GAT CTT TTC
416 GTG GAA CTC TTG ATG ACA TTC TGA AGA AAA ACG ATC CAG ATT TCA CAT TAA
417 CCT CTG GTT ATG AAG AAA GAA AGA TCA ACG ACC TGG AGG CAA AGC TCC
418 TCT CTG AGA TCG ACA AGG TAG CTG AGC TGG AAG ATC ACA TTC AGC AGC
419 TCC GTC AAG AAC TTG ACG ACC AAT CTG CAA GGC TTG CCG ATT CAG AAA ATG

420 TTC GCG CTC AGC TTG AAG CGG CCA CTG GAC AAG GAA TCC TCG GAG CTG
421 CTG GAA ACG CTA TGG TTC CAA ATT CAA CGT TCA TGA TCG GGA ACG GTC
422 GTG AAT CAC AGA CGC GAG ACC AGC TCA ATT ACA TTG ATG ATC TTG AAA CGA
423 AGT TAG CTG ATG CGA AGA AGG AAA ATG ATA AGG CTC GTC AGG CAC TCG
424 TTG AAT ACA-3′.

425 **Western blotting**

426 45 adult worms were picked and transferred to blank plates for 20 min to remove bacteria
427 from their bodies. Worms were then moved to PCR tubes containing 10 µl of milli-Q water
428 to which 10 µl of SDS loading buffer was added. Samples were separated by SDS-PAGE.
429 Protein from each gel was transferred to a nitrocellulose membrane using a Trans-blot
430 turbo transfer for high molecular weight proteins (10 min). Membranes were incubated in
431 a blocking buffer consisting of TBS-T + 3% Blotting-Grade Blocker (BioRad) shaking at
432 room temperature for 1 hr. Membranes were then washed three times with TBS-T and
433 incubated shaking with primary antibodies overnight at 4°C. The primary antibody was
434 washed off three times with TBS-T and incubated with secondary antibodies at room
435 temperature for 1 hr. Each membrane was then incubated in ECL reagent (Thermo Fisher
436 Scientific SuperSignal West Femto) for 5 min and imaged with a ChemiDoc Touch
437 Imaging System. Primary antibodies: Mouse anti-alpha tubulin (Product No: 3873S;
438 1:1,000; Cell Signaling Technologies); Rabbit anti-SPD-5 C-terminus (1:1,000, clone 785,
439 Dresden Antibody Facility; Pelletier et al., 2004). Secondary Antibodies (1:50,000 for all):
440 HRP conjugated Goat anti-Rabbit IgG (1 mg/ml) (catalog No: 65-6120, catalog No:
441 J276300; Invitrogen); HRP conjugated Goat anti-Mouse (1.5 mg/ml) (Catalog No: 62-
442 6520, Catalog No: WA312227; Invitrogen); and HRP conjugated Donkey anti-Goat (1
443 mg/ml) (Catalog No: A15999, Catalog No: 58-155-072318; Invitrogen).

444 **Microscopy of *C. elegans* embryos**

445 Embryos from adult worms were dissected on a 22 × 22 mm coverslip (Catalog No: 2975-
446 225; Coring) using a 22-gauge needles in a 7 µl solution of egg salts buffer (ESB) (118mM
447 NaCl, 48mM KCl, 2mM $CaCl_2$, 2mM $MgCl_2$, 25mM Hepes) or M9 buffer. Samples were
448 then mounted onto plain 25 × 75 × 1 mm microscope slides (Catalog No: 12-544-4; Fisher

449 Scientific). Time-lapse images were acquired with an inverted Nikon Eclipse Ti2-E
450 microscope with a Yokogawa confocal scanner unit (CSU-W1), piezo Z stage, and an
451 iXon Ultra 888 EMCCD camera (Andor), controlled by Nikon Elements software. We used
452 a 100X Plan Apo silicon immersion objective (NA 1.35). To quantify GFP::SPD-5
453 transgene intensity we imaged at 15-18 × 1-µm Z-stacks using 488-nm at 2 x 2 binning,
454 15% laser power, 100 ms exposures every 20 seconds until centrosome disassembly
455 except where specified.

456 For microtubule depolymerization assays, one-cell embryos from adult worms were
457 treated with ESB mixed with nocodazole to make a 40 µM nocodazole solution or 2%
458 DMSO solution and imaged prior to PNM. For SPD-5 growth curves one-cell embryos
459 from adult worms were dissected in M9 and imaged prior to pronuclear meeting (PNM).

460 ***In vivo* partial FRAP of centrosomes**

461 One-cell embryos from adult worms were dissected in M9 buffer and photobleached with
462 a 405-nm laser at NEBD using a stim point positioned in the center of centrosomes at 1%
463 intensity, 50 ms dwell time. To quantify the intensity of GFP::SPD-5 transgene after
464 photobleaching a 5 µm line scan was positioned at centrosomes such that the maximum
465 and minimum intensity occurred at 1.82 µm and 2.6 µm respectively. GFP::SPD-5
466 transgene intensity was recorded immediately after photobleaching and 100 s thereafter.
467 Intensities are averaged over replicates and normalized to the maximum intensity
468 immediately after photobleaching.

469 **Centrosome extrusion assay**

470 Dissected one-cell embryos from adult worms were coated in a solution of 10 µm
471 Calcofluor-white (Biotium catalog No: 29067) in ESB or MQ H2O. To extrude
472 centrosomes, a 405 nm laser was targeted to the periphery of the eggshell using (100%
473 laser intensity, 500 ms dwell time). Cell cycle stage was determined by chromosome
474 organization via mCherry::H2B signal. Imaging was performed as above with a 60 × 1.2
475 NA Plan Apochromat water-immersion objective, GFP/mCherry splitter, 2 x 2 binning, 488
476 nm laser (15% intensity), 561 nm laser (10% intensity), 51 x 0.5 µm Z-steps, every 2 min
477 for 60 min or until centrosomes completely dissolved. The integrated density of

478 GFP::SPD-5 was normalized to centrosome intensity prior to extrusion in the normalized
479 plot.

480 **96-well glass bottom passivation**

481 To clean a 96-well glass bottom imaging plate, wells were then treated with a solution of
482 5% v/v Hellmanex (Sigma-Aldrich catalog No: Z805939) for 1hr and washed 10X in H2O
483 and dried. A solution of 5M NaOH is added to wells for 1hr and washed 5X with H2O. To
484 passivate the surface of the wells, the 96-well glass-bottom imaging plate was treated
485 with a solution of 0.5% w/v of mPEG-Silane, MW 5,000 (Creative PEGWorks catalog No:
486 PLS-2011) in 95% EtOH for 1hr and then washed 10X with H2O and dried. On the day of
487 the experiment, a solution of 5% w/v of Bovine Serum Albumin (BSA) (Sigma-Aldrich)
488 was incubated in the wells for 30 min, washed 5X with H2O and then dried.

489

490 ***In vitro* PCM scaffold reconstitution and imaging**

491 To reconstitute PCM scaffold assembly from purified components we incubated 1μM
492 SPD-5::RFP, 1μM TPXL-1::GFP, 75mM KCl, 1mM DTT, 0.4mM ATP, 1mM $MgCl_2$,4mM
493 Hepes pH 7.4, except where indicated, in a passivated 96-well glass-bottom imaging plate
494 for 15 min. To prevent evaporation wells are covered with parafilm (Bemis). To image
495 reconstituted PCM we used at 100x silicon objective an inverted Nikon Eclipse Ti2-E
496 microscope with a Yokogawa confocal scanner unit (CSU-W1), piezo Z stage, and an
497 iXon Ultra 888 EMCCD camera (Andor), controlled by Nikon Elements software. Imaging
498 was performed at 488-nm; 2 x 2 binning, 1% intensity, 100ms exposure, and 561-nm; 1x1
499 binning, 5% intensity, 100ms exposure at a single imaging plane at the surface of the
500 glass except where specified. For condensate FRAP and fusion assays, we imaged at
501 0.5 x 10μm relative to the surface of the glass well.

502 ***In vitro* PCM scaffold FRAP assay**

503 To measure the dynamics of reconstituted PCM scaffolds, we incubated samples (as
504 above) with 0.5 μM PLK-1(CA) or 0.5 μM PLK-1(KD) for 30 minutes and then
505 photobleached with a 405 nm laser using a rectangular ROI positioned within
506 condensates at 20% intensity, 200 μs dwell time. We imaged condensates at 0.5 x 10 μm

507 relative to the surface of the glass well. The mean intensity of SPD-5::RFP and TPXL-
508 1::GFP was recorded prior to photobleaching and recorded every 15 seconds for 10 min
509 post photobleaching. Mean intensities were normalized to mean intensity prior to
510 photobleaching. 6 and 5 replicated were performed for PLK-1(KD) and PLK-1(CA)
511 conditions respectively.

512 ***In vitro* PCM scaffold dilution assay**

513 To determine the sensitivity to dilution of reconstituted PCM, we prepared reconstituted
514 PCM scaffolds using 1μM SPD-5::RFP, 1μM TPXL-1::GFP, 50mM KCl, 1mM DTT,
515 0.4mM ATP, 1mM $MgCl_2$,4mM Hepes pH 7.4 and incubated with 0.5 μM PLK-1(CA) or
516 0.5 μM PLK-1(KD) in a cleaned non-passivated 96-well glass imaging plate. Samples
517 were incubated for 1hr and Imaged. Samples were then diluted samples with 4.3x
518 extrusion buffer (150mM KCl, 25mM Hepes pH 7.4) and incubated for an additional hour
519 and imaged. We measured the integrated density of SPD-5::RFP prior and after dilution
520 in which 6 images at different locations at the surface of the glass well were gathered for
521 each condition.

522 ***In vitro* PCM scaffold assembly assay**

523 To determine the effect of PLK-1 phosphorylation on the assembly of reconstituted PCM
524 scaffolds, we incubated 1μM SPD-5::GFP, 1μM TPXL-1, 50mM KCl, 1mM DTT, 0.4mM
525 ATP, 1mM $MgCl_2$, 4mM Hepes pH 7.4 with 0.5μM PLK-1(CA) or 0.5μM PLK-1(KD) in a
526 passivated 96-well imaging plate. We imaged using 488-nm; 2 x 2 binning, 1% intensity,
527 100ms exposure. 3 images at distinct locations at the surface of the glass well were
528 recorded at every interval for intervals 5, 10, 15, 20, 30, 45, 60, 90 minutes from one
529 experiment for PLK-1(CA) and PLK-1(KD). Condensate size was measured using a semi-
530 automated threshold-based analysis. The watershed function in FIJI was used to
531 segregated chains of condensates.

532

533 **Video particle tracking sample preparation and analysis**

534 Samples were prepared in 384-well glass bottom microwell plates (Brooks Life Science
535 Systems: MGB101-1-2-LK-L). Prior to use, the plates were cleaned with 5% Hellmanex

536 III (Hëlma Analytics), etched with 1M KOH, and siliconized with Sigmacote (Sigma-
537 Aldrich). On the day of the experiment, individual wells were blocked with 1% bovine
538 serum albumin, then rinsed thoroughly with MilliQ-water. PCM samples were prepared
539 with 1 μM SPD-5::GFP, 1 μM TPXL-1, 50 mM KCl, 0.4 mM ATP, 1 mM $MgCl_2$,1mM
540 Hepes pH 7.4 pH), 150 beads/μL with 0.2 μM PLK-1(KD) or 0.2 μM PLK-1(CA) and 100
541 nm-diameter carboxylate-modified fluorescent beads (Invitrogen: F8801). The final
542 concentration of beads was <150 beads/μL. Samples were incubated inside the
543 temperature-controlled microscope chamber at 30°C for at least 1 hour before imaging.

544 **Video particle tracking microrheology microscopy**

545 Images were captured on a Lecia DMI6000 B microscope base with a Yokogawa CSU-
546 X1 spinning disk confocal scanner unit and a 405/488/561/647 nm Laser Quad Band Set
547 filter cube (Chroma) with a plan apo 63 or 100 × 1.40 NA oil immersion objective. Images
548 were acquired using a Hamamatsu ImagEMX2 EM-CCD camera at 15ms/frame using
549 stream acquisition function on Metamorph (Biovision) software. At least 10000 frames (3-
550 25 min) were acquired for each acquisition, up to 6 acquisitions were made per sample
551 per session, and at least 3 sessions were carried out per sample for reproducibility.

552 **Video particle tracking microrheology analysis**

553 Particle tracking and calculation of mean squared displacement (MSD) was performed
554 using MATLAB codes by Daniel Blair & Eric Dufresne
555 (https://site.physics.georgetown.edu/matlab/code.html). Average MSD was calculated
556 from >17000 individual trajectories and smoothed using a moving average with span
557 <10% of total number of frames. Elastic (G') and viscous (G") moduli as a function of
558 frequency (ω) were calculated from the averaged MSD from 0.015 to 100s using
559 generalized Stokes-Einstein relation (GSER) as described by Mason TG (Rheologica
560 Acta, 2000) using MATLAB codes by Andrew Sun
561 (https://github.com/andrewx101/track_analysis/releases/tag/v2.05). Viscosity (η) is
562 calculated (η = G"/ω) and plotted against frequency. From viscosity plot, the mean value
563 of the plateau at the low frequency was used to estimate the zero-shear viscosity (η_0).

564 **Image quantification and statistical analysis**

565 Images were analyzed using a semiautomated, threshold-based particle analysis in FIJI
566 (https://fiji.sc/). MATLAB (Mathworks) was used to analyze VPT experiments. All data are
567 expressed as the mean ± 95% confidence intervals as stated in the figure legends and
568 results. The value of n and what n represents (e.g., number of centrosomes, condensates
569 or experimental replicates) is stated in figure legends and results. A Brown-Forsythe and
570 Welch ANOVA statistical test were used for normally distributed data, and a Kruskal-Walis
571 were used for non-normally distributed data. Significance was reported as; p value < 0.05
572 = *, p value < 0.005 = **, p value < 0.0005 = ***, p value of < 0.00005 = ****.

573

574 **TABLE S1. Baculoviral expression constructs for protein expression.**

protein	**sequence**	**plasmid name**	**parent plasmid (pOCC #)**	**N-term tag**	**C-term tag**	**species**
SPD-5	Full-length	JWV1	pOCC28	MBP-PreScission	eGFP-PreScission-6xHis	*C.elegans*
SPD-5	Full-length	JWV3	pOCC25	MBP-PreScission	RFP-PreScission-6xHis	*C.elegans*
TPXL-1	Full-length	JWV29	pOCC27	MBP-PreScission	eGFP-PreScission-6xHis	*C.elegans*
TPXL-1	Full-length	JWV30	pOCC28	MBP-PreScission	PreScission-6xHis	*C.elegans*
PLK-1(CA)	Full-length T194D	JWV11	pOCC7	6xHis-Prescission	-	*C.elegans*
PLK-1(KD)	Full-length K67M	JWV12	pOCC7	6xHis-Prescission	-	*C.elegans*

575

576

577 **TABLE S2. C. elegans strains.**

Strain name	genotype	Creation method	Origin
JWW12	unc-119(ed9) III; ltSi202[pVV103/ pOD1021; Pspd-2::GFP::SPD-5 RNAiresistant;cb-unc-119(+)]II	MosSCI into EG6699	(Woodruff et al., 2015)
JWW69	unc-119(ed9) III; ltSi202[pVV103/ pOD1021; Pspd-2::GFP::SPD-5 re-encoded;cb-unc-119(+)]II; ltIs37 [(pAA64) pie-1p::mCherry::his-58 + unc-119(+)] IV.	MosSCI into EG6699	This study
JWW70	unc-119(ed9) III; utsw1[pJWB56; Pspd-2::GFP::SPD-5(530E, 627E, 653E, 658E) re-encoded; cb-unc-119(+)]II; ltIs37 [(pAA64) pie-1p::mCherry::his-58 + unc-119(+)] IV.	MosSCI into EG6699	This study
JWW94	mCherry::his-58, unc-119(ed9) III; ltSi228[pVV153/ pOD1615; Pspd-2::GFP::spd-5 S530A,S627A, S653A, S658A reencoded; cb-unc-119(+)]II	MosSCI into EG6699	(Woodruff et al., 2015)

578

579

580 **FIGURE LEGENDS**

581 **Figure 1: The *C. elegans* PCM scaffold is a composite of distinct but coexisting**
582 **stable and dynamic phases.**

583 a. Diagram of centrosome release and dilution via extrusion. *C. elegans* embryos
584 were coated with calcofluor white and eggshells were ruptured with a 405 nm laser.
585 b. Representative images of centrosomes (labeled with GFP::SPD-5) extruded from
586 a one-cell embryo at metaphase into low salt buffer (0mM KCl, 25mM Hepes pH
587 7.4). DNA is labeled with H2B::mCherry.
588 c. Representative images of centrosomes extruded from one-cell embryos different
589 cell cycle stages into high salt buffer (150mM KCl, 25mM Hepes pH 7.4).
590 d. Quantification of integrated density of GFP::SPD-5 of extruded centrosomes
591 imaged every 2 minutes for 1 hr (mean +/- 95% C.I.; interphase n=11, metaphase
592 n=12, anaphase n=9 centrosomes)
593 e. Normalized data from D).
594

595 **Figure 2: Phosphorylation of SPD-5 regulates the equilibrium of the dynamic and**
596 **stable PCM scaffold components.**

597 a. Top, diagram of key PLK-1 phosphorylation sites in SPD-5. Bottom, design of
598 *gfp::spd-5* transgenes expressed at the Mos locus on chromosome II.
599 b. Left, centrosomes were extruded from metaphase embryos expressing *gfp::spd-5*
600 transgenes (no RNAi). High salt buffer was used (150mM KCl, 25mM Hepes, pH
601 7.4). Right, quantification of the integrated density of GFP::SPD-5 of extruded
602 centrosomes imaged every 2 minutes for 1 hr (mean +/- 95% C.I.; SPD-5(WT) n=
603 12, SPD-5(4A) n=9, SPD-5(4E) n=5 centrosomes).
604 c. Partial fluorescence recovery after photobleaching (FRAP) of centrosomes in
605 intact embryos. Centrosomes were photobleached at nuclear envelop breakdown
606 in one-cell embryos expressing *gfp::spd-5* transgenes (no RNAi). GFP intensity
607 was measured with a 5 μm line scan 0 s and 100 s after photobleaching (mean +/-
608 95% C.I.; GFP::SPD-5(WT) n= 16, GFP::SPD-5(4E) n=8, GFP::SPD-5(4A) n=7
609 centrosomes).

610

611 **Figure 3: PLK-1 phosphorylation changes the dynamics of reconstituted PCM**
612 **scaffolds.**

613 a. Reconstitution of PCM condensates using purified SPD-5, TPXL-1, and no
614 molecular crowding agent. Proteins were assembled for 15 min in buffer (75 mM
615 KCl, 4 mM Hepes pH 7.4, 10 mM DTT, 0.4 mM ATP, 1 mM $MgCl_2$) and imaged in
616 a 96-well glass bottom plate using confocal fluorescence microscopy.
617 b. PLK-1 phosphorylation affects the morphological properties of reconstituted PCM
618 scaffolds. Samples were prepared as in (A) with 0.5 μM kinase dead PLK-1(KD)
619 or 0.5 μM constitutively active PLK-1(CA) and imaged after 30 min. Top panel,
620 static images. Bottom panel, timelapse imaging of condensates. Arrows indicate
621 the site of condensate fusion.
622 c. Fluorescence recovery after photobleaching of SPD-5/TPXL-1 condensates. Top,
623 SPD-5::RFP intensity was measured and normalized (mean +/- 95% C.I.). PLK-
624 1(KD) n = 6, PLK-1(CA) n = 6 condensates). Bottom, images of bleached
625 condensates.
626 d. Dilution assay of reconstituted PCM. 1 μM SPD-5::RFP, 1 μM TPXL-1::GFP was
627 incubated in buffer (50 mM KCl, 4 mM Hepes pH 7.4, 10 mM DTT, 0.4 mM ATP,
628 1 mM $MgCl_2$) with 0.5 μM PLK-1 (KD) or 0.5 μM PLK-1(CA) for 1 hr and imaged.
629 Samples were then diluted 4.3X into extrusion buffer (150mM KCl, 25mM Hepes
630 pH.7.4) and imaged after 1 hr (left panels). Right, quantification of SPD-5::RFP
631 integrated density before and after dilution (mean +/- 95% C.I.; PLK-1(KD) n=6
632 images, PLK-1 (CA) n=6 images with >100 condensates).

633

634 **Figure 4: Phosphorylation increases the viscoelasticity of reconstituted PCM**
635 **scaffolds**

636 a. Schematic of Video Particle Tracking (VPT) technique. 100 nm-diameter
637 carboxylate-modified fluorescent beads were encapsulated in reconstituted
638 PCM condensates. Left, representative confocal fluorescence image. Top right,
639 diagram of condensate with bead; not to scale. Bottom right, representative
640 trajectory of a single bead within a condensate.

641 b. Plot for averaged mean squared displacement (MSD) of beads encapsulated
642 in reconstituted PCM condensates. PCM condensates were incubated with 0.2
643 μM PLK-1(KD) or 0.2 μM PLK-1(CA).
644 c. Plots for viscoelastic moduli of condensates determined from VPT. Moduli were
645 calculated from using the generalized Stokes-Einstein relation (GSER) fit to a
646 maxwell fluid from the averaged MSD from 0.015 to 100 s (shaded region in
647 panel B). Dashed line indicates crossover frequency.
648 d. Viscosity was calculated from averaged MSD from 0.015 to 100 s (shaded
649 region in B). The mean value of the plateau at the low frequency was used to
650 estimate the zero-shear viscosity (η_0).
651 e. Summary of rheological measurements.
652
653 **Figure 5: Hypo-phosphorylation of SPD-5 impairs PCM strength and the fidelity of**
654 **chromosome segregation.**
655 a. Transgenic worms were treated with *spd-5* RNAi to silence expression of
656 endogenous SPD-5. Left, one-cell embryos expressing GFP::SPD-5(WT) or
657 GFP::SPD-5(4A) treated with 2% DMSO or 40 μM nocodazole at nuclear envelope
658 breakdown. Right, quantification of PCM area and PCM integrated density (mean
659 +/- 95% C.I.; WT + DMSO n = 24, WT+ nocodazole n=26, 4A + DMSO n=26, 4A
660 + nocodazole n=26; p values from Brown-Forsythe and Welch ANOVA tests).
661 b. Time-lapse images of transgenic embryos (+s*pd-5(RNAi)*) during mitosis. DNA is
662 visualized with H2B::mCherry.
663 c. Chromosome segregation defects seen in embryos solely expressing GFP::SPD-
664 5(4A).

665 **Figure 6: Hyper-phosphorylation of SPD-5 limits PCM scaffold growth.**
666 a. PCM assembly in one-cell embryos expressing GFP::SPD-5 transgenes in the
667 presence of endogenous SPD-5. Top, representative images taken at nuclear
668 envelope breakdown (NEBD). Bottom, quantification of GFP::SPD-5 integrated
669 density relative to NEBD (mean +/- 95% C.I.; WT n=22, 4E n=22 centrosomes)

670 b. As in A), except worms were treated with RNAi to deplete endogenous SPD-5
671 (mean +/- 95% C.I.; WT n=18, 4E n=30 centrosomes)
672 c. PCM size at NEBD after microtubules were depolymerized with nocodazole.
673 (mean +/- 95% C.I.; WT n=20, 4E n=12, 4E + *spd-5(RNAi)* n=18; p values from a
674 Kruskal-Wallis test).
675 d. Chromosome segregation in embryos expressing GFP::SPD-5(4E).
676 e. Embryo viability assay (mean +/- 95% C.I.; WT n=8, WT + *spd-5(RNAi)* n=8, 4E
677 n=7, 4E + *spd-5(RNAi)* n=8 mothers, >20 embryos counted per mother; p values
678 from a Kruskal-Wallis test).
679 f. *In vitro* PCM condensate assembly assay over time. Right, representative images.
680 Left, quantification of average condensate size over time (mean +/- 95% C.I.;
681 n>100 condensates from 3 replicates).
682
683 **Figure 7: Phospho-regulated tuning of viscoelastic properties balances PCM**
684 **growth and strength.**
685 a. Diagram of PCM architecture in a *C. elegans* embryo. The PCM scaffold comprises
686 two forms of interconnected SPD-5 molecules: a dynamic, liquid-like fraction
687 (orange) and a stable, solid-like fraction (red). Conversion between states is driven
688 by phosphorylation and dephosphorylation of SPD-5. PCM must grow while
689 resisting pulling forces mediated by microtubules.
690 b. Balance of stable and dynamic SPD-5 scaffolds is needed for proper PCM function.
691 Left, under-phosphorylation of SPD-5 leads to PCM that is too dynamic and weak,
692 and it gets quickly pulled apart by forces. Right, over-phosphorylation of SPD-5
693 makes the PCM scaffold too solid-like, which prevents full-scale PCM growth and
694 hinders late embryonic development.
695
696 **SUPPLEMENTAL FIGURE LEGENDS**
697 **Figure S1. In vitro analysis of PCM.**
698 a. Coomassie gel of proteins used in this study.

699 b. Reconstituted PCM condensates. Representative images of reconstituted PCM
700 condensates prepared with 1 μM SPD-5::RFP, 1 μM TPXL-1::GFP, 50 mM KCl,
701 Hepes pH 7.4 and incubated for 15 min.
702 c. Fluorescence recovery after photobleaching (FRAP) of reconstituted PCM
703 condensates incubated with 0.5 μM PLK-1(KD) or 0.5 μM PLK-1(CA) for 30 min.
704 TPXL-1::GFP intensity was measured and normalized (mean +/- 95% C.I.; KD, n
705 = 5, CA n = 6 condensates).
706
707 **Figure S2. *In vivo* analysis of SPD-5(4E).**
708 a. Western blot against SPD-5. Alpha tubulin was detected as a loading control.
709 Worms were grown at 23°C
710 b. Plot of cell cycle length in one-cell embryos expressing GFP::SPD-5 transgenes.
711 Time from pronuclear meeting (PNM) to nuclear envelope breakdown (NEBD) was
712 measured (mean +/- 95% C.I. p values from Kruskal-Wallis test).
713
714 **REFERENCES**

715 Alberti, S., and A.A. Hyman. 2021. Biomolecular condensates at the nexus of cellular
716 stress, protein aggregation disease and ageing. *Nat Rev Mol Cell Biol*. 22:196-213.
717 Boke, E., M. Ruer, M. Wuhr, M. Coughlin, R. Lemaitre, S.P. Gygi, S. Alberti, D. Drechsel, A.A.
718 Hyman, and T.J. Mitchison. 2016. Amyloid-like Self-Assembly of a Cellular
719 Compartment. *Cell*. 166:637-650.
720 Bose, M., M. Lampe, J. Mahamid, and A. Ephrussi. 2022. Liquid-to-solid phase transition of
721 oskar ribonucleoprotein granules is essential for their function in Drosophila
722 embryonic development. *Cell*. 185:1308-1324 e1323.
723 Conduit, P.T., Z. Feng, J.H. Richens, J. Baumbach, A. Wainman, S.D. Bakshi, J. Dobbelaere,
724 S. Johnson, S.M. Lea, and J.W. Raff. 2014. The centrosome-specific phosphorylation
725 of Cnn by Polo/Plk1 drives Cnn scaffold assembly and centrosome maturation. *Dev*
726 *Cell*. 28:659-669.
727 Decker, M., S. Jaensch, A. Pozniakovsky, A. Zinke, K.F. O'Connell, W. Zachariae, E. Myers,
728 and A.A. Hyman. 2011. Limiting amounts of centrosome material set centrosome
729 size in C. elegans embryos. *Curr Biol*. 21:1259-1267.
730 Enos, S.J., M. Dressler, B.F. Gomes, A.A. Hyman, and J.B. Woodruff. 2018. Phosphatase
731 PP2A and microtubule-mediated pulling forces disassemble centrosomes during
732 mitotic exit. *Biol Open*. 7.
733 Feng, Z., A. Caballe, A. Wainman, S. Johnson, A.F.M. Haensele, M.A. Cottee, P.T. Conduit,
734 S.M. Lea, and J.W. Raff. 2017. Structural Basis for Mitotic Centrosome Assembly in
735 Flies. *Cell*. 169:1078-1089 e1013.

736 Gomes Pereira, S., M.A. Dias Louro, and M. Bettencourt-Dias. 2021. Biophysical and
737 Quantitative Principles of Centrosome Biogenesis and Structure. *Annu Rev Cell Dev*
738 *Biol*. 37:43-63.
739 Hamill, D.R., A.F. Severson, J.C. Carter, and B. Bowerman. 2002. Centrosome maturation
740 and mitotic spindle assembly in C. elegans require SPD-5, a protein with multiple
741 coiled-coil domains. *Dev Cell*. 3:673-684.
742 Haren, L., T. Stearns, and J. Luders. 2009. Plk1-dependent recruitment of gamma-tubulin
743 complexes to mitotic centrosomes involves multiple PCM components. *PLoS One*.
744 4:e5976.
745 Laan, L., N. Pavin, J. Husson, G. Romet-Lemonne, M. van Duijn, M.P. Lopez, R.D. Vale, F.
746 Julicher, S.L. Reck-Peterson, and M. Dogterom. 2012. Cortical dynein controls
747 microtubule dynamics to generate pulling forces that position microtubule asters.
748 *Cell*. 148:502-514.
749 Laos, T., G. Cabral, and A. Dammermann. 2015. Isotropic incorporation of SPD-5 underlies
750 centrosome assembly in C. elegans. *Curr Biol*. 25:R648-649.
751 Lee, K., and K. Rhee. 2011. PLK1 phosphorylation of pericentrin initiates centrosome
752 maturation at the onset of mitosis. *J Cell Biol*. 195:1093-1101.
753 Lemaitre, R.P., A. Bogdanova, B. Borgonovo, J.B. Woodruff, and D.N. Drechsel. 2019.
754 FlexiBAC: a versatile, open-source baculovirus vector system for protein
755 expression, secretion, and proteolytic processing. *BMC Biotechnol*. 19:20.
756 Lucas, E.P., and J.W. Raff. 2007. Maintaining the proper connection between the centrioles
757 and the pericentriolar matrix requires Drosophila centrosomin. *J Cell Biol*. 178:725-
758 732.
759 Magescas, J., J.C. Zonka, and J.L. Feldman. 2019. A two-step mechanism for the
760 inactivation of microtubule organizing center function at the centrosome. *Elife*. 8.
761 Megraw, T.L., K. Li, L.R. Kao, and T.C. Kaufman. 1999. The centrosomin protein is required
762 for centrosome assembly and function during cleavage in Drosophila.
763 *Development*. 126:2829-2839.
764 Mittasch, M., V.M. Tran, M.U. Rios, A.W. Fritsch, S.J. Enos, B. Ferreira Gomes, A. Bond, M.
765 Kreysing, and J.B. Woodruff. 2020. Regulated changes in material properties
766 underlie centrosome disassembly during mitotic exit. *J Cell Biol*. 219.
767 Nakajo, M., H. Kano, K. Tsuyama, N. Haruta, and A. Sugimoto. 2022. Centrosome
768 maturation requires phosphorylation-mediated sequential domain interactions of
769 SPD-5. *J Cell Sci*. 135.
770 Ohta, M., Z. Zhao, D. Wu, S. Wang, J.L. Harrison, J.S. Gomez-Cavazos, A. Desai, and K.F.
771 Oegema. 2021. Polo-like kinase 1 independently controls microtubule-nucleating
772 capacity and size of the centrosome. *J Cell Biol*. 220.
773 Pecreaux, J., J.C. Roper, K. Kruse, F. Julicher, A.A. Hyman, S.W. Grill, and J. Howard. 2006.
774 Spindle oscillations during asymmetric cell division require a threshold number of
775 active cortical force generators. *Curr Biol*. 16:2111-2122.
776 Putnam, A., M. Cassani, J. Smith, and G. Seydoux. 2019. A gel phase promotes
777 condensation of liquid P granules in Caenorhabditis elegans embryos. *Nat Struct*
778 *Mol Biol*. 26:220-226.

Ranganathan, S., and E.I. Shakhnovich. 2020. Dynamic metastable long-living droplets formed by sticker-spacer proteins. *Elife*. 9.

Rios, M.U., M.A. Bagnucka, B.D. Ryder, B. Ferreira Gomes, N.E. Familiari, K. Yaguchi, M. Amato, W.E. Stachera, L.A. Joachimiak, and J.B. Woodruff. 2024. Multivalent coiled-coil interactions enable full-scale centrosome assembly and strength. *J Cell Biol*. 223.

Schnackenberg, B.J., A. Khodjakov, C.L. Rieder, and R.E. Palazzo. 1998. The disassembly and reassembly of functional centrosomes in vitro. *Proc Natl Acad Sci U S A*. 95:9295-9300.

Sun, T.L., T. Kurokawa, S. Kuroda, A.B. Ihsan, T. Akasaki, K. Sato, M.A. Haque, T. Nakajima, and J.P. Gong. 2013. Physical hydrogels composed of polyampholytes demonstrate high toughness and viscoelasticity. *Nat Mater*. 12:932-937.

Tollervey, F., M.U. Rios, E. Zagoriy, J.B. Woodruff, and J. Mahamid. 2024. Native molecular architectures of centrosomes in C. elegans embryos. *bioRxiv*.

Wang, Z., T. Wu, L. Shi, L. Zhang, W. Zheng, J.Y. Qu, R. Niu, and R.Z. Qi. 2010. Conserved motif of CDK5RAP2 mediates its localization to centrosomes and the Golgi complex. *J Biol Chem*. 285:22658-22665.

Woodruff, J.B., B. Ferreira Gomes, P.O. Widlund, J. Mahamid, A. Honigmann, and A.A. Hyman. 2017. The Centrosome Is a Selective Condensate that Nucleates Microtubules by Concentrating Tubulin. *Cell*. 169:1066-1077 e1010.

Woodruff, J.B., and A.A. Hyman. 2015. Method: In vitro analysis of pericentriolar material assembly. *Methods Cell Biol*. 129:369-382.

Woodruff, J.B., O. Wueseke, V. Viscardi, J. Mahamid, S.D. Ochoa, J. Bunkenborg, P.O. Widlund, A. Pozniakovsky, E. Zanin, S. Bahmanyar, A. Zinke, S.H. Hong, M. Decker, W. Baumeister, J.S. Andersen, K. Oegema, and A.A. Hyman. 2015. Centrosomes. Regulated assembly of a supramolecular centrosome scaffold in vitro. *Science*. 348:808-812.

Figure 1

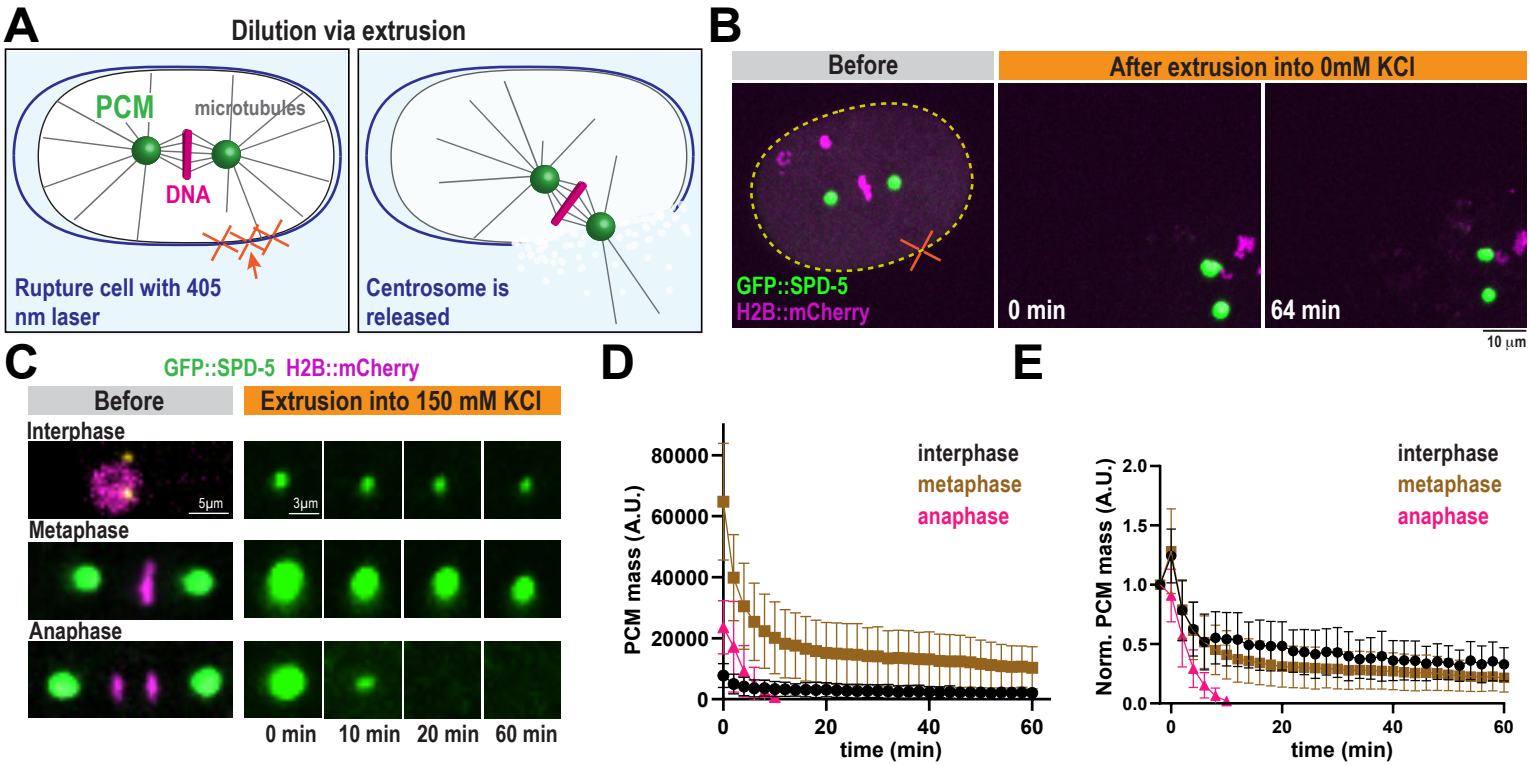
A
Dilution via extrusion
PCM
microtubules
DNA
Rupture cell with 405 nm laser
Centrosome is released
B
Before
After extrusion into 0mM KCl
GFP::SPD-5
H2B::mCherry
0 min
64 min
10 µm
C
GFP::SPD-5 H2B::mCherry
Before
Extrusion into 150 mM KCl
Interphase
Metaphase
Anaphase
5µm
3µm
0 min
10 min
20 min
60 min
D
PCM mass (A.U.)
time (min)
interphase
metaphase
anaphase
E
Norm. PCM mass (A.U.)
time (min)
interphase
metaphase
anaphase

Figure 2

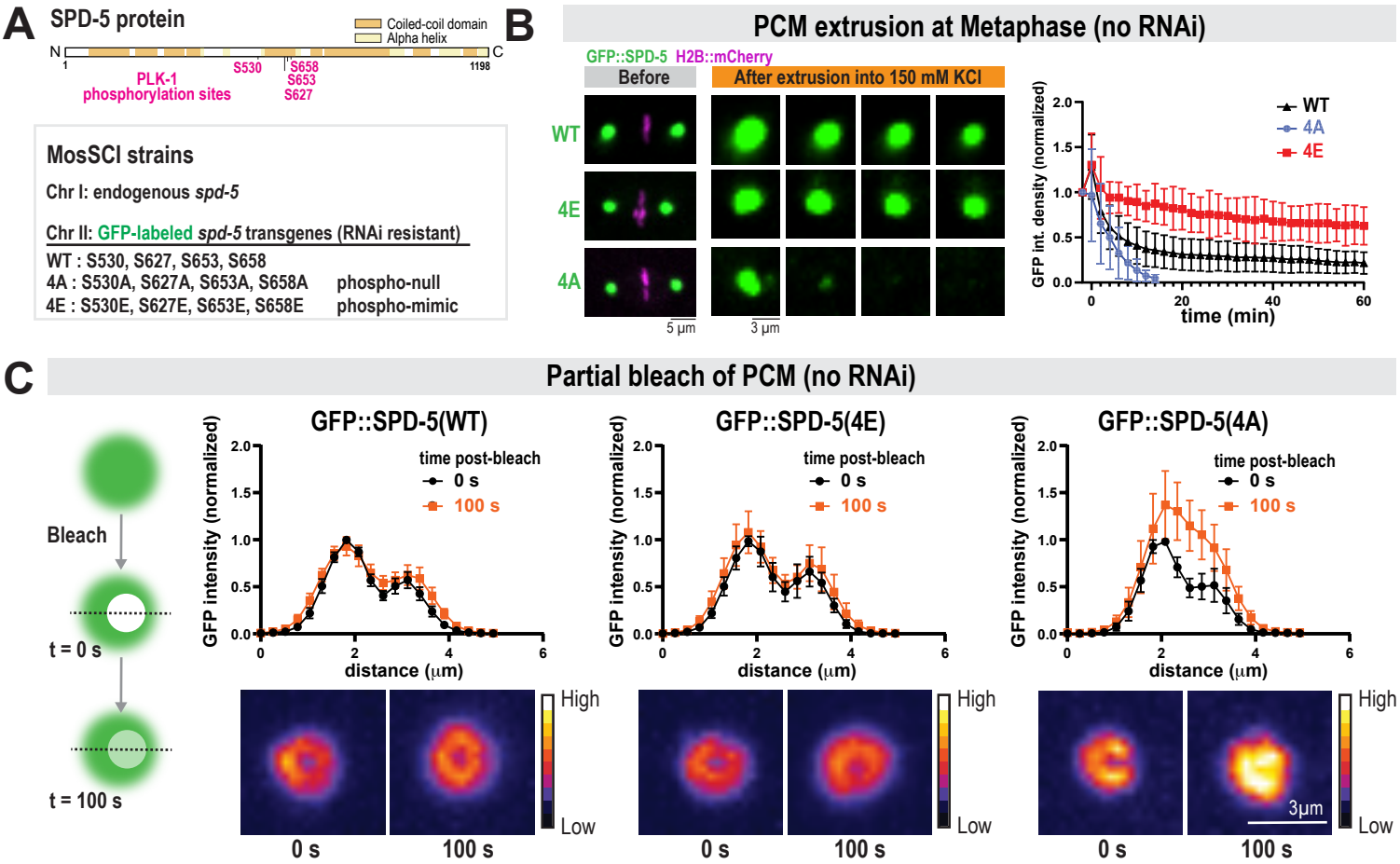
A
SPD-5 protein
Coiled-coil domain
Alpha helix
N
C
1
1198
S530
S658
S653
S627
PLK-1
phosphorylation sites
MosSCI strains
Chr I: endogenous spd-5
Chr II: GFP-labeled spd-5 transgenes (RNAi resistant)
WT : S530, S627, S653, S658
4A : S530A, S627A, S653A, S658A phospho-null
4E : S530E, S627E, S653E, S658E phospho-mimic
B
PCM extrusion at Metaphase (no RNAi)
GFP::SPD-5 H2B::mCherry
Before
After extrusion into 150 mM KCl
WT
4E
4A
5 µm
3 µm
GFP int. density (normalized)
time (min)
WT
4A
4E
C
Partial bleach of PCM (no RNAi)
Bleach
t = 0 s
t = 100 s
GFP::SPD-5(WT)
GFP::SPD-5(4E)
GFP::SPD-5(4A)
GFP intensity (normalized)
distance (µm)
time post-bleach
0 s
100 s
High
Low
3µm

Figure 3

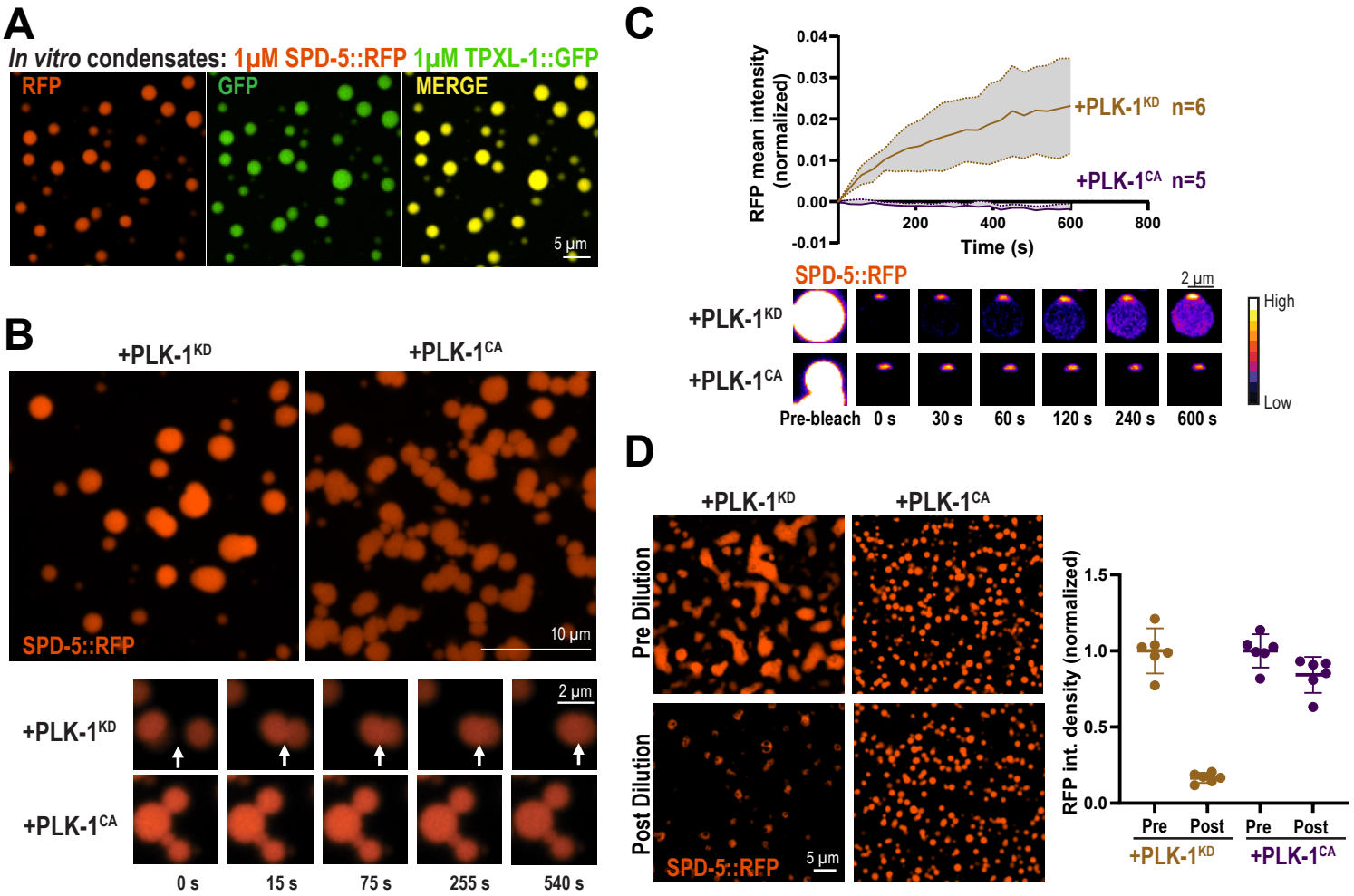
A
In vitro condensates: 1µM SPD-5::RFP 1µM TPXL-1::GFP
RFP
GFP
MERGE
5 µm
B
+PLK-1KD
+PLK-1CA
SPD-5::RFP
10 µm
2 µm
+PLK-1KD
+PLK-1CA
0 s
15 s
75 s
255 s
540 s
C
RFP mean intensity (normalized)
0.04
0.03
0.02
0.01
0.00
-0.01
200
400
600
800
Time (s)
+PLK-1KD n=6
+PLK-1CA n=5
SPD-5::RFP
2 µm
High
Low
+PLK-1KD
+PLK-1CA
Pre-bleach
0 s
30 s
60 s
120 s
240 s
600 s
D
+PLK-1KD
+PLK-1CA
Pre Dilution
Post Dilution
SPD-5::RFP
5 µm
RFP int. density (normalized)
1.5
1.0
0.5
0.0
Pre
Post
Pre
Post
+PLK-1KD
+PLK-1CA

Figure 4

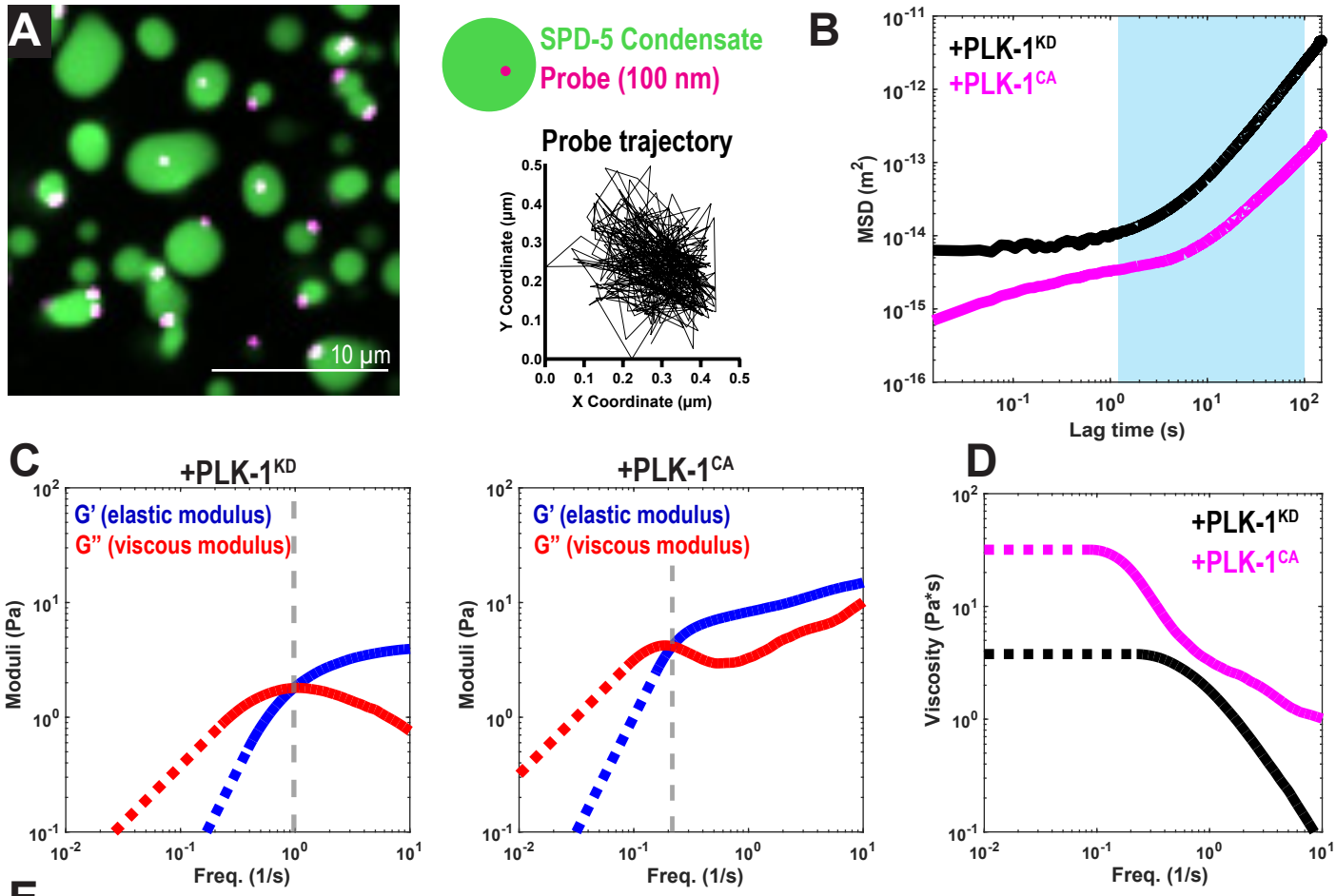

E

PLK-1	Crossover Point (1/s)	Zero Shear Viscosity (Pa•s)	Relaxation Time (s)	Condensate Fusion?	Material State
KD	0.975	3.779	1.026	yes	more liquid-like
CA	0.217	31.84	4.616	no	more solid-like

Figure 5

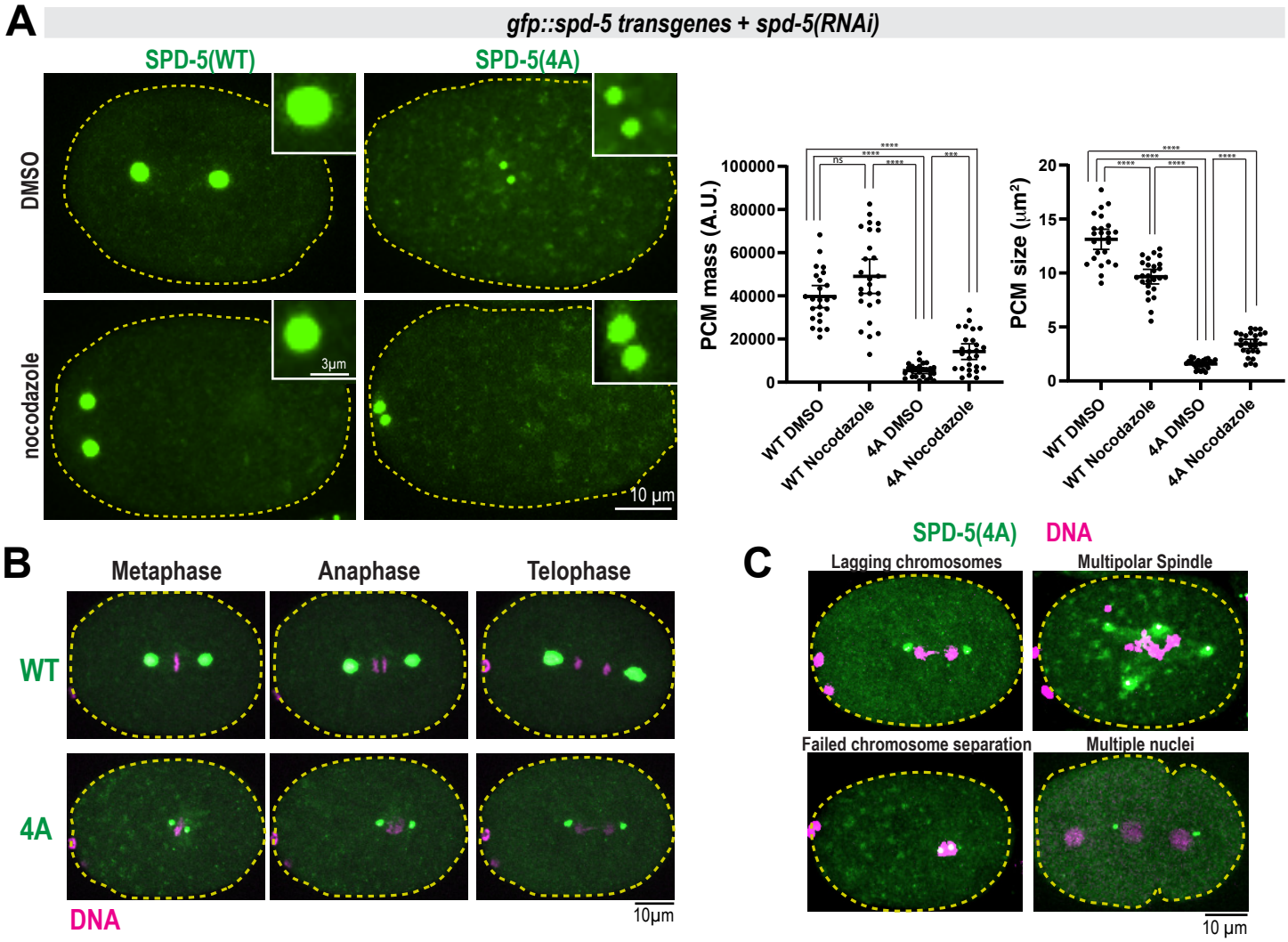
A
gfp::spd-5 transgenes + spd-5(RNAi)
SPD-5(WT)
SPD-5(4A)
DMSO
nocodazole
3µm
10 µm
PCM mass (A.U.)
PCM size (µm²)
WT DMSO
WT Nocodazole
4A DMSO
4A Nocodazole
B
Metaphase
Anaphase
Telophase
WT
4A
DNA
10µm
C
SPD-5(4A)
DNA
Lagging chromosomes
Multipolar Spindle
Failed chromosome separation
Multiple nuclei
10 µm

Figure 6

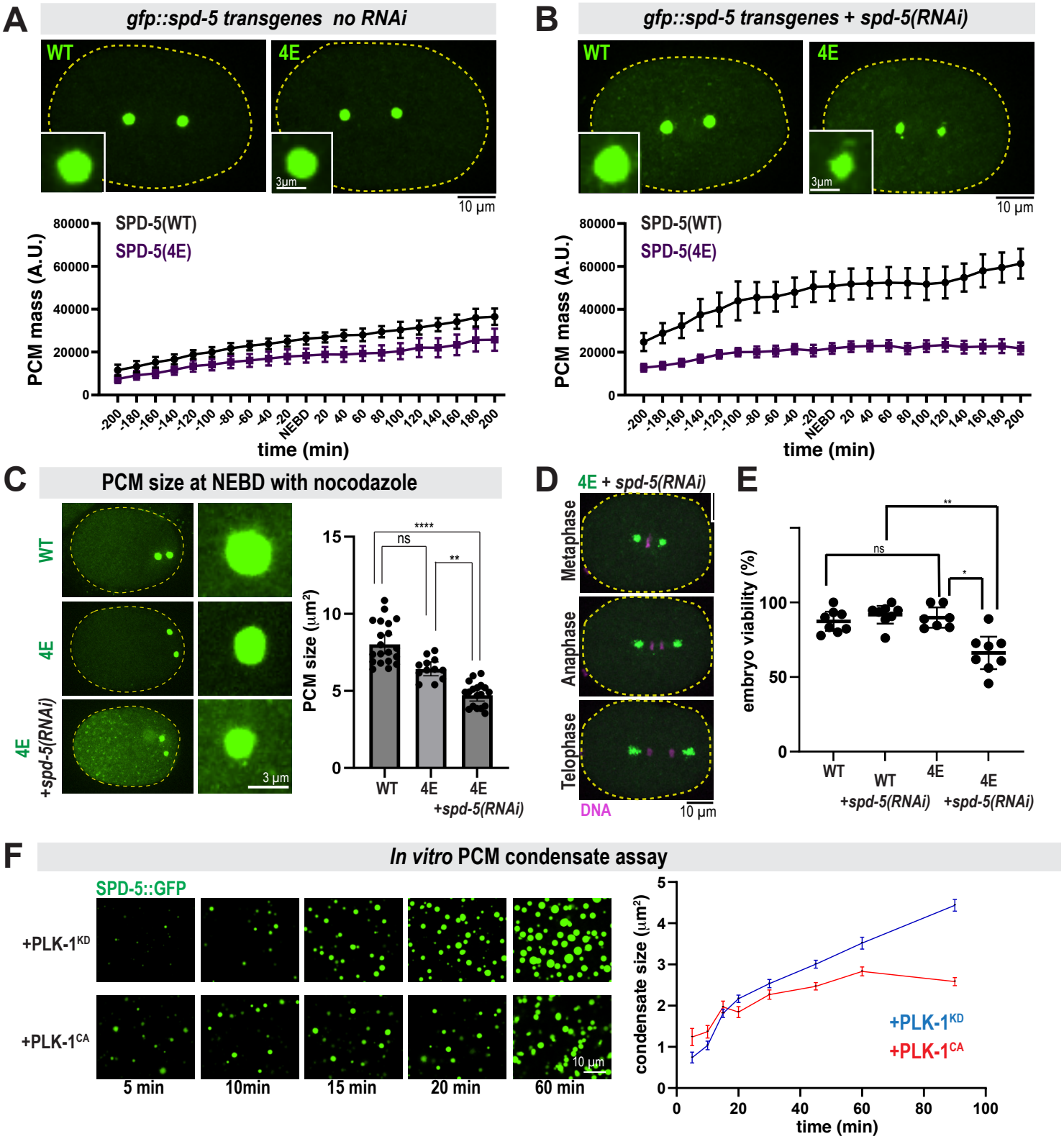
A
gfp::spd-5 transgenes no RNAi
WT
4E
3µm
10 µm
SPD-5(WT)
SPD-5(4E)
PCM mass (A.U.)
time (min)
B
gfp::spd-5 transgenes + spd-5(RNAi)
C
PCM size at NEBD with nocodazole
4E +spd-5(RNAi)
3 µm
PCM size (µm²)
ns
****
**
WT
4E
4E +spd-5(RNAi)
D
4E + spd-5(RNAi)
Metaphase
Anaphase
Telophase
DNA
E
embryo viability (%)
*
WT +spd-5(RNAi)
4E +spd-5(RNAi)
F
In vitro PCM condensate assay
SPD-5::GFP
+PLK-1KD
+PLK-1CA
5 min
10min
15 min
20 min
60 min
condensate size (µm²)

Figure 7

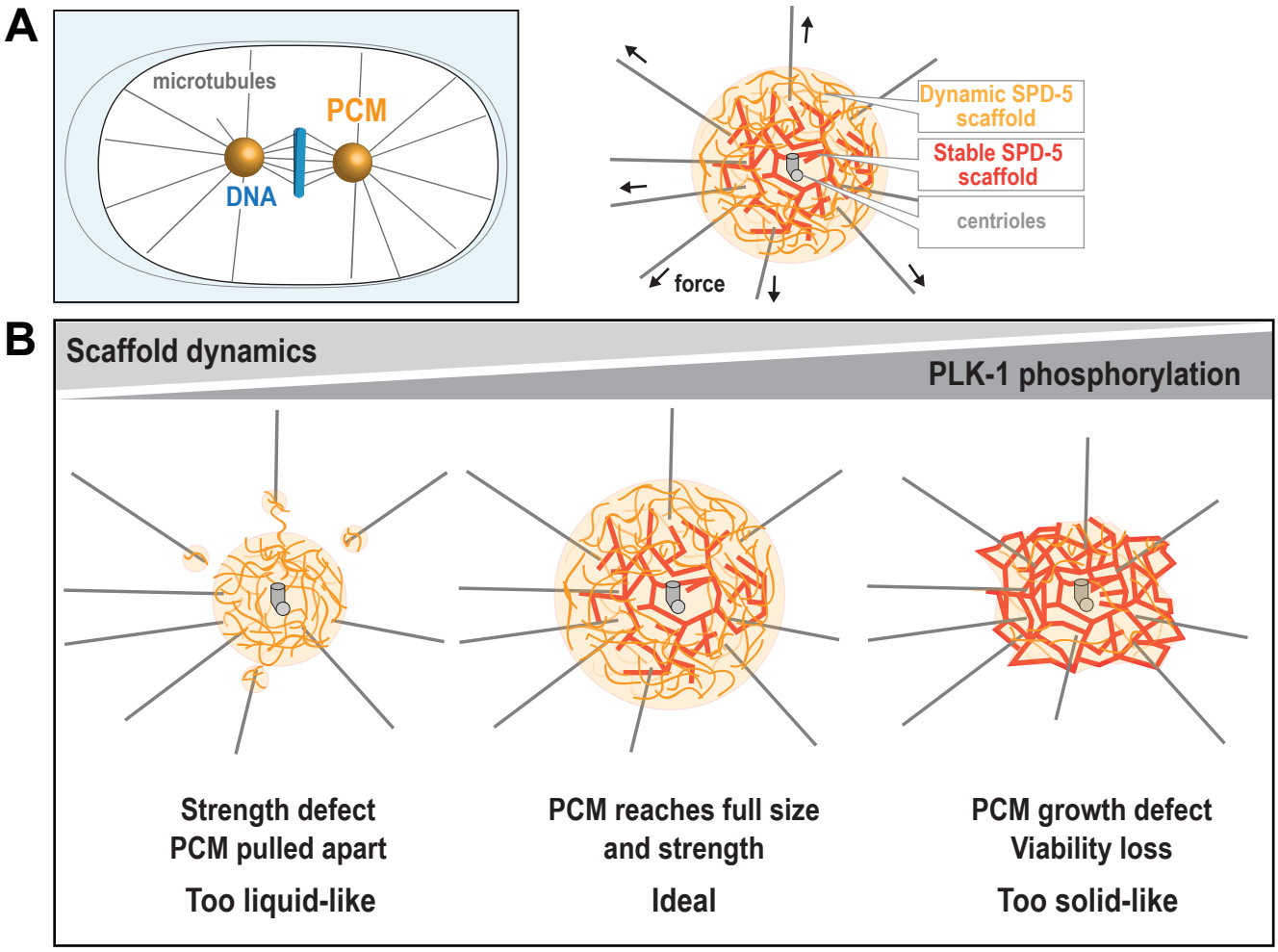
A
microtubules
PCM
DNA
Dynamic SPD-5 scaffold
Stable SPD-5 scaffold
centrioles
force
B
Scaffold dynamics
PLK-1 phosphorylation
Strength defect
PCM pulled apart
Too liquid-like
PCM reaches full size
and strength
Ideal
PCM growth defect
Viability loss
Too solid-like

Figure S1

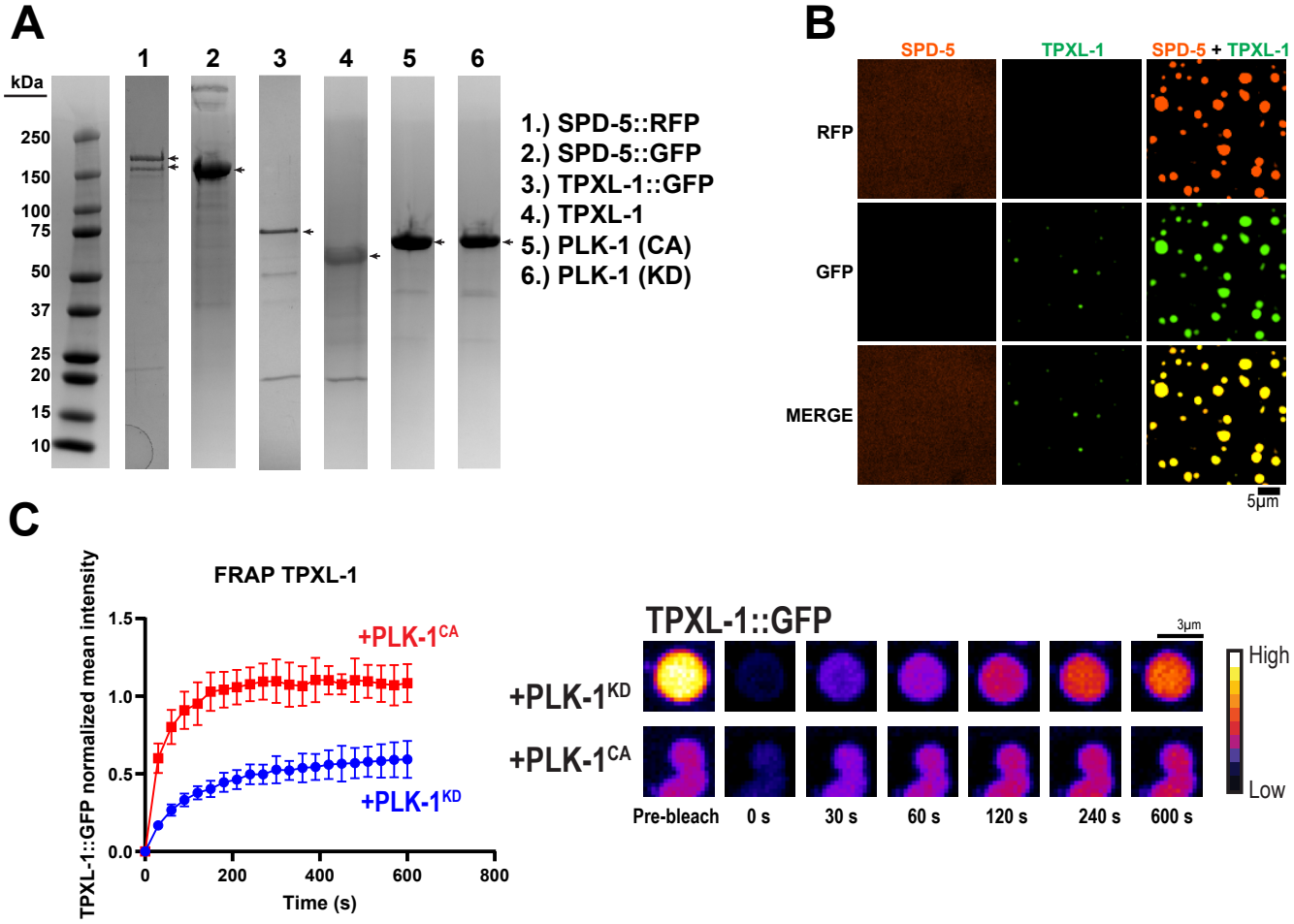
A
kDa
250
150
100
75
50
37
25
20
15
10
1
2
3
4
5
6
1.) SPD-5::RFP
2.) SPD-5::GFP
3.) TPXL-1::GFP
4.) TPXL-1
5.) PLK-1 (CA)
6.) PLK-1 (KD)
B
SPD-5
TPXL-1
SPD-5 + TPXL-1
RFP
GFP
MERGE
5µm
C
FRAP TPXL-1
TPXL-1::GFP normalized mean intensity
Time (s)
+PLK-1CA
+PLK-1KD
TPXL-1::GFP
3µm
High
Low
+PLK-1KD
+PLK-1CA
Pre-bleach
0 s
30 s
60 s
120 s
240 s
600 s

Figure S2

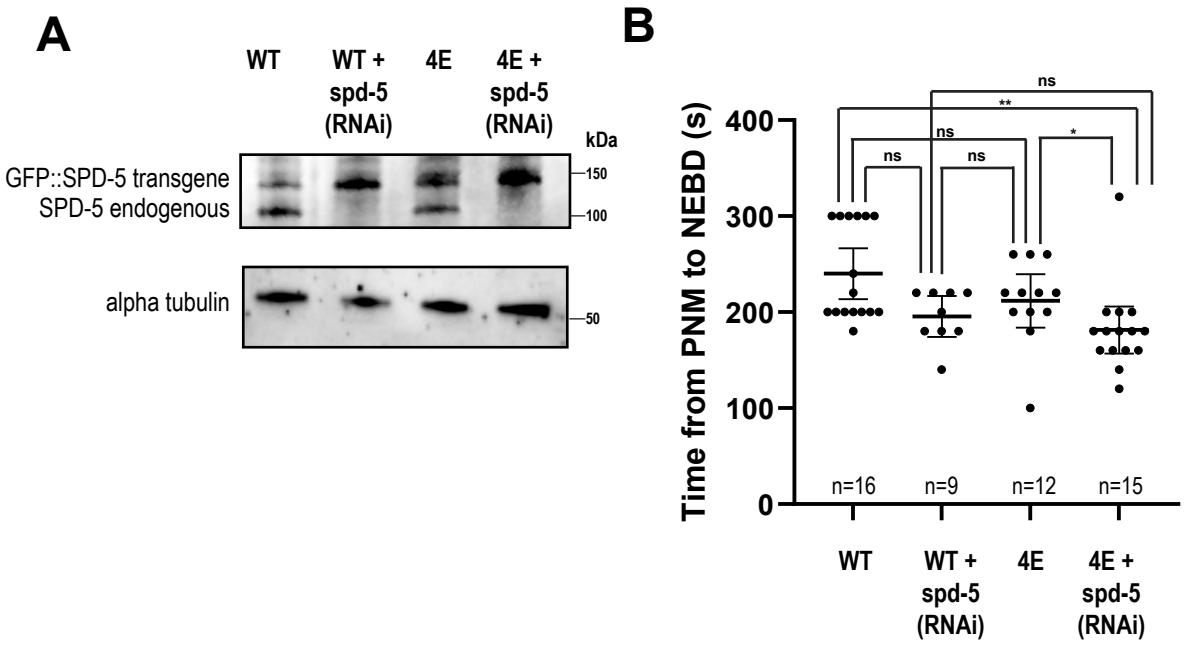
A
WT
WT + spd-5 (RNAi)
4E
4E + spd-5 (RNAi)
kDa
GFP::SPD-5 transgene
SPD-5 endogenous
150
100
alpha tubulin
50
B
Time from PNM to NEBD (s)
400
300
200
100
0
ns
**
ns
ns
ns
*
n=16
n=9
n=12
n=15
WT
WT + spd-5 (RNAi)
4E
4E + spd-5 (RNAi)